RSC Sustainability

ROYAL SOCIETY OF CHEMISTRY

PAPER

View Article Online
View Journal | View Issue

Cite this: *RSC Sustainability*, 2026, **4**, 1393

Production of magnesium ferrite for use as phosphate adsorbents in water

Matheus Henrique Pimentel Araújo, *[a] Laura Melo Fernandes Moreira, [a] José Domingos Ardisson,[b] Rochel Monteiro Lago[c] and Juliana Cristina Tristão*[a]

In this study, magnesium ferrite was synthesised at different calcination temperatures (300, 700, and 900 °C), and its phosphate adsorption potential was evaluated. TG, XRD, Mössbauer spectroscopy, and VSM data indicate the formation of the magnesium ferrite phase, $MgFe_2O_4$, in the inverted spinel and mixed spinel structures at different calcination temperatures, exhibiting superparamagnetic characteristics. Adsorption studies indicate that the presence of $MgFe_2O_4$ favours phosphate adsorption, and the magnetic properties facilitate the recovery of the adsorbents by approaching magnets. The phosphate adsorption isotherm curves obtained for the materials MgFe700 and MgFe900 indicate that adsorption occurs at specific sites, attributed to Mg and Fe on the surface of the material, with a better fit for the Temkin and Langmuir isothermal models, respectively. The kinetic tests indicate two stages of adsorption, the first with fast adsorption and the second with a slower process. The data exhibit a better fit to the Elovich kinetic model, indicating that chemisorption occurs on the material's surface with specific adsorption sites. Phosphate adsorption tests show that the materials can be applied in a wide pH range (3 to 10) and in the presence of anions such as Cl^-, NO_3^-, and HCO_3^-, commonly present in natural and wastewater, with adsorption capacities between 16 and 30 mg g^{-1} for MgFe700 and between 19 and 28 mg g^{-1} for MgFe900. The desorption tests of the materials revealed a strong interaction between the adsorbent and adsorbate, hindering the release of phosphate adhered to the material's surface and, consequently, leading to a low reuse rate.

Received 29th August 2025
Accepted 26th December 2025

DOI: 10.1039/d5su00715a

rsc.li/rscsus

Sustainability spotlight

Developing effective materials for water decontamination remains a priority. Phosphorus, a vital agricultural nutrient often lost as waste, must be recovered to support food security (SDG 2), reduce aquatic pollution (SDG 6), and promote responsible production (SDG 12). This work focused on synthesising magnesium ferrite *via* a lower-energy process and evaluating its phosphate removal effectiveness. The material exhibits strong binding to phosphate, which is key to permanently eliminating it from aquatic environments, albeit at the expense of a lower reuse rate. These findings advance the understanding of phosphorus adsorption dynamics in iron and magnesium-based materials, informing the design of future adsorbents for sustainable applications.

Introduction

Phosphorus (P) is an essential element for life and is crucial for various biochemical processes and plant growth. It is a vital nutrient for food production and is absorbed in the form of phosphate (PO_4^{3-}). Under ideal conditions, PO_4^{3-} is not present in high concentrations in natural water due to the low solubility of its minerals and its endogenous biogeochemical cycle.[1–4] However, human activities such as mining, agriculture, industrial processes, and the dumping of household waste into rivers, lakes, and seas have altered the natural P cycle, causing its concentration to increase. Consequently, the imbalance can lead to eutrophication and deterioration of water quality, resulting in toxicological effects and the death of animals and plants due to a lack of sufficient dissolved oxygen.[5–8]

In this context, recovering phosphate from natural waters is crucial for preventing environmental issues and enhancing global food security.[8,9] Several processes for removing this contaminant have been studied and applied, including biological action through the activity of microorganisms and plants, chemical precipitation methods, and sorption reactions of clays and oxides.[10] The adsorption process is an effective option for removing various pollutants due to its low cost, minimal sludge generation, ease of application, and the potential for recovering and reusing the adsorbent material.[4] Iron-based materials (Fe)

[a]*Universidade Federal de Viçosa – Campus Florestal – UFV, Rodovia LMG 818, km 06, s/n, Campus Universitário, Florestal, MG, 35690-000, Brazil. E-mail: matheus.pimentel@ufv.br*

[b]*Centro de Desenvolvimento da Tecnologia Nuclear – CDTN/CNEN, Campus da Universidade Federal de Minas Gerais, Avenida Presidente António Carlos, No 6627, Rua Mário Werneck, S/N – Pampulha, Belo Horizonte, MG, Brazil*

[c]*Universidade Federal de Minas Gerais – UFMG, Avenida Presidente António Carlos, No 6627, Rua Mário Werneck, 2 – Pampulha, Belo Horizonte, MG, 31270-901, Brazil*

have emerged as promising adsorbents, particularly those with magnetic properties, as they facilitate removal after application.[11,12]

Among Fe-based magnetic materials, ferrites have proven to be highly versatile in biomedical applications, photocatalysis, contaminant degradation, and toxic metal adsorption, among others.[13–21] It is noted that the most common ferrites contain toxic metals, such as Cu, Ni and Co, and replacing them with more abundant and environmentally safe metals can bring benefits. As in the use of zinc ferrites ($ZnFe_2O_4$) for removing phosphate from water, which yielded results of around 5.2 mg g^{-1} and exhibited interesting magnetic properties.[6] Alkaline earth metals, such as Ca and Mg, are also viable options, with the potential to form ferrites with various crystalline structures.

Materials based on calcium and magnesium, supported or in bulk, have been applied in recent years for the removal of phosphate from water. Layered double hydroxides of Ca–Mg, Mg–Al, brucite and periclase, as well as alternative materials such as eggshell, can be used for the recovery of phosphate from water.[22–28] The element Mg has a high charge density and a small ionic radius, which may be related to its high affinity for phosphate.[25] The formation of magnesium ferrites from the combustion method favours the adsorption of phosphate with values of 16.2 and 12.3 mg g^{-1}.[29] Magnesium ferrite, together with biochar production, increased the phosphate adsorption capacity and facilitated the recovery of the material after magnetic separation.[30]

The recovery and reapplication of adsorbents are essential to consider the technical and economic viability of the materials and to assess the environmental impact resulting from their use. Magnetic properties in adsorbent materials can reduce costs, leading to great interest in the study of ferrite-based materials as adsorbents for various contaminants.[31–33] In addition to magnetic recovery through an approach to a magnet, these particles have the potential to be regenerated and reused. Once the phosphate is adsorbed on the surface of the material, it needs to be extracted for other purposes, and the adsorbent material is recovered for reuse. Different extracting solutions can be applied to remove the adsorbed phosphate. Among them, solutions containing bases such as KOH and NaOH[5,34,35] stand out, and solutions containing $NaHCO_3$/Na_2CO_3.[35–37] Magnesium ferrite exhibits excellent magnetic properties, facilitating the recovery and reuse of materials after the adsorption process, thereby enabling the reapplication of the material.

This work aimed to synthesise magnesium ferrite ($MgFe_2O_4$) *via* a simple, environmentally safe thermal decomposition route without organic precursors, under different calcination conditions (300 °C, 700 °C, and 900 °C for 1 h). The magnetic materials were comprehensively characterised to evaluate the effect of calcination temperature on the formation of the spinel structure and the resulting structural and magnetic properties. Phosphate adsorption tests were conducted to determine optimal conditions and propose a possible mechanism for PO_4^{3-} removal. This study presents a new synthesis approach focusing on the modulation of these properties, in which detailed characterisation enabled direct correlation between spinel structures and phosphate adsorption efficiency. The reuse of adsorbent materials was also studied under different conditions to evaluate their reapplication potential and the potential for controlled phosphate release.

Methods

Materials synthesis

The magnetic adsorbent materials were synthesised by the thermal decomposition method without organic precursors. The direct thermal decomposition method, without organic precursors or hydroxides, was chosen because it is a simplified, more sustainable synthesis route that aims to reduce CO_2 emissions during calcination. The salts magnesium nitrate hexahydrate ($Mg(NO_3)_2 \cdot 4H_2O$ – Vetec) and iron nitrate nonahydrate ($Fe(NO_3)_3 \cdot 9H_2O$ – Neon) were used as precursors in the molar ratio Mg : Fe 1 : 1 and solubilised in 50 mL of deionised water. The precursor mixture was heated to 90 °C under magnetic stirring to evaporate the solvent, and then it was kept in an oven at approximately 90 °C for 12 h. The resulting material was calcined in a tubular furnace (Sanchis 1200) at temperatures of 300, 700, and 900 °C for 1 h with a heating rate of 5 °C min^{-1}. Calcination was performed at three different temperatures (300, 700, and 900 °C) to investigate the influence of energy input on ferrite properties. The upper range was defined by the literature, which indicates temperatures above 600 °C to ensure spinel phase crystallisation and desired magnetic properties.[38,39] The codes used to identify the samples are shown in Table 1. After calcination, the materials were washed with deionised water in a water-to-sample (mL : mg) ratio of four times and dried in an oven at 70 °C for 12 hours.

Materials characterisation

The synthesised materials were characterised by different techniques to evaluate the influence of the calcination temperature on the formation of magnesium ferrite. Thermogravimetric analysis (TG) was used to assess the thermal stability and decomposition of the precursors used. The analysis was conducted in compressed air with a flow rate of 50 mL min^{-1} at a heating rate of 10 °C min^{-1}, ranging from room temperature to 900 °C in a Shimadzu TG/DTA equipment (model DTG-60H).

The materials were characterised by X-ray diffraction to identify the crystalline phases formed at different temperatures. The diffractograms were obtained in a SHIMADZU diffractometer (XRD-7000 X-ray), Kα Cu radiation $\lambda = 1.5406$ Å, voltage 30.0 kV, current 30.0 mA in continuous scanning from 4° to 70° 2θ at a speed of 4° min^{-1}. The diffractograms obtained were analysed in the Profex software to identify the phases according to the

Table 1 Sample identification codes

Annealing temperature	RT[a]	300 °C	700 °C	900 °C
Samples code	MgFe	MgFe300	MgFe700	MgFe900

[a] RT – room temperature.

Crystallography Open Database (COD).[40] The average crystallite size was calculated using the Scherrer equation.

Through Mössbauer spectroscopy, the iron phases present in the samples were identified, and the hyperfine parameters were calculated. The Mössbauer spectra for ^{57}Fe were obtained at 23 K, with a ^{57}Co/Rh source. The hyperfine parameters and isometric shifts (IS) were calculated using the Normos software calibrated according to Fe (α-Fe) standards.

The morphology and elemental composition of the synthesised materials were observed using scanning electron microscopy (SEM) and energy-dispersive spectroscopy (EDS). The SEM images, spectra, and chemical maps obtained by EDS were acquired using the Quanta 200 FEG equipment. To study the magnetic properties of the synthesised materials, a vibrating sample magnetometer (VSM) was used. The VSM hysteresis curves were obtained by a Lakeshore VSM model 7404 at room temperature, under a magnetic field of 1.8 tesla (18 kOe). The BET surface area was determined through N_2 adsorption/desorption isotherms using Autosorb 1 Quantachrome equipment, and the data were obtained using the ASiQwin 5.21 software.

The influence of the pH of the medium on the surface charge of the materials was studied by determining the point of zero charge (pH_{PZC}). The pH_{PZC} was defined following the adapted methodology of Freitas *et al.* (2015).[41] For each pH value analysed 20 mg of the adsorbent material was weighed in duplicate. The pH range varied from 1 to 14. Each Erlenmeyer flask containing the adsorbent material was increased by 10 mL of 0.1 mol per L KCl solution. The pH value was adjusted by decreasing the volume of 0.1 mol per L HCl (9 mL to 1 mL) and increasing the volume of 0.1 mol per L NaOH (1 mL to 9 mL), thereby completing the final volume to 20 mL with deionised water. The initial pH was measured, and the flasks were maintained at 100 rpm for 24 h in an incubator (Novatecnica N715). Finally, the pH was calculated again, and a pH_{final} *versus* $pH_{initial}$ curve was constructed. The formation of bonds on the surface of the materials was studied by infrared (IR). The infrared spectra were obtained for the samples before and after adsorption using a PerkinElmer FTIR equipment in ATR with a scanning range of 400 to 4000 cm^{-1} and a resolution of 4 cm^{-1}, eight scans, in an air-conditioned room at 21 °C. The leaching of Mg and Fe during washing was evaluated by atomic absorption (AA) analyses of the supernatant. Data were acquired using Varian equipment (Model AA740 FS) with hollow cathode lamps for Mg and Fe.

Phosphate adsorption tests (PO_4^{3-})

The materials were tested as phosphate adsorbents under various conditions and in triplicate. First, an adsorption experiment was performed using all adsorbents to measure the adsorption capacity (q_e) of each one and select the most suitable materials. The adsorption tests were conducted in batches with polypropylene conical tubes containing 15 mg of material and 15 mL of phosphate solution. The phosphate solution with an initial concentration (C_i) of 50 mg per L (KH_2PO_4 – Vetec) was prepared from a 1000 mg per L standard solution. The vials were kept under orbital agitation at 150 rpm for 24 h at room temperature. At the end, the samples were centrifuged for 15 min at 3900 rpm (FANEM) and filtered through a 0.22 μm syringe filter (KASVI). The equilibrium concentration (C_e) was determined by the ascorbic acid method described in the Standard Methods for the Examination of Water and Wastewater.[42] The readings were taken on a Micronal AJX 1000 spectrophotometer with a λ of 880 nm in glass cuvettes with a 1 cm optical path. This method was used as a standard for phosphate determination in the pH, competition, isotherm, kinetics and desorption/reuse tests.

Isotherm experiments

The isotherm experiment was conducted to determine the maximum adsorption capacity of the selected materials and to elucidate part of the adsorption mechanism. For this purpose, 15 mg of material and 15 mL of PO_4^{3-} solution at different concentrations (C_i = 10, 25, 50, 75, 100, 125, 150, 200, 250 mg L^{-1}) were used. The polypropylene tubes were kept under agitation at 200 rpm for 24 h at 25 °C in an incubator (Novatecnica N715). The amount of phosphate was determined by the ascorbic acid method. Three different isotherm models were applied to evaluate the adsorption mechanism, using models that evaluate two isotherm parameters: Langmuir, Freundlich and Temkin. The Redlich–Peterson model, which assesses three isothermal parameters, was also applied. The nonlinear equations used are in the SI Table S1.

Kinetic experiments

To better understand how the selected materials adsorb substances and to clarify the adsorption process, we conducted adsorption kinetics experiments on the MgFe700 and MgFe900 samples. During the experiments, 100 mg of material was kept in contact with 100 mL of PO_4^{3-} solution (50 mg L^{-1}) in an Erlenmeyer flask at 150 rpm, 25 °C. Aliquots of 1 mL were withdrawn at predetermined intervals: 0, 10, 20, 30, 45, 60, 90, 120, 180, 240, 300, 360, 540, 720, 1440, 2160, 2880 min and the amount of phosphate was determined by the ascorbic acid method. The data were analysed according to the pseudo-first-order, pseudo-second-order, and Elovich kinetic models; the nonlinear equations are provided in Table S2.

pH influence and selectivity

In the second step, the previously selected materials were tested under new conditions. The influence of the initial pH (pH_i) on the adsorption test was studied by changing the pH_i of different phosphate solutions (C_i 50 mg L^{-1}) by adding drops of NaOH (0.1 mol L^{-1}) or HCl (0.1 mol L^{-1}) solution, until obtaining pH_i of 3, 5, 7, 9 and 11.

The selectivity of the materials for phosphate under the influence of various ions during the adsorption process was investigated. Solutions containing phosphate and the competing ion (SO_4^{2-}, NO_3^{2-}, HCO_3^-, Cl^- or CO_3^{2-}) were prepared, both at a concentration of 50 mg L^{-1}. For both the pH influence and selectivity tests, the flasks were kept under orbital agitation at 150 rpm for 24 h at room temperature. Finally, the

samples were centrifuged for 15 min at 3900 rpm (FANEM) and filtered through a 0.22 μm syringe filter. The phosphate adsorption capacity was measured using the method described before.

Phosphate desorption tests and reuse of adsorbent materials

To evaluate the reusability of the materials, phosphate desorption tests were conducted, applying four different extracting solutions, varying the alkaline medium and ionic strength. To evaluate desorption in an alkaline medium, 1 and 0.5 mol per L NaOH solutions were used. To study the influence of ionic strength on desorption, 0.1 and 0.01 mol per L KCl solutions were used. Initially, the phosphate adsorption test was conducted as described in the previous sessions, with the only change being the contact time, which was to 12 hours. Then, for desorption, 15 mL of extracting solution was added to the tube containing 15 mg of material. After contact with the phosphate solution, the tubes were incubated for 12 h at 150 rpm and 25 °C with a desorbent solution of NaOH or KCl. After this time, the concentration of desorbed phosphate was determined by the ascorbic acid method.[42] With this experiment, the optimal desorption condition was identified and subsequently applied to the reuse of the material. The magnetic property of the materials was used in the reuse step. During the supernatant separation process, the tubes were kept close to a neodymium magnet to retain the solid within the tube, preventing material loss during cycles and allowing analysis of the supernatant. Four adsorption/desorption cycles were conducted to investigate the reusability and reapplication capacity of the materials, with the adsorption capacity being determined at each cycle.

Results and discussion

The adsorbent materials were characterised using various techniques to analyse their thermal and magnetic behaviour, identify the crystalline phases formed, and evaluate important textural properties relevant to the adsorption process.

Thermal analysis (TG/DTG)

The thermal decomposition curve of the MgFe material, before being subjected to calcination, can be a combination of the decomposition of the two precursors. Previous work has shown that the precursor magnesium nitrate hexahydrate $Mg(NO_3)_2 \cdot 6H_2O$ is more thermally stable than the iron nitrate nonahydrate $Fe(NO_3)_3 \cdot 9H_2O$.[43–45]

Three main events in the decomposition of the MgFe material are observed (Fig. 1). The first event occurs between 20 and 170 °C with a loss of approximately 30.1% in mass. This event may relate to the loss of residual water molecules from the drying process of the precursors and the hydration water of the precursors $Fe(NO_3)_3 \cdot 9H_2O$ and $Mg(NO_3)_2 \cdot 4H_2O$. The most significant contribution is that iron nitrate nonahydrate loses all water molecules up to 150 °C, and is completely dehydrated before 200 °C. The second event occurs between 170 and 270 °C, resulting in a loss of approximately 7.9% by mass. This event may be associated with the completion of the decomposition of

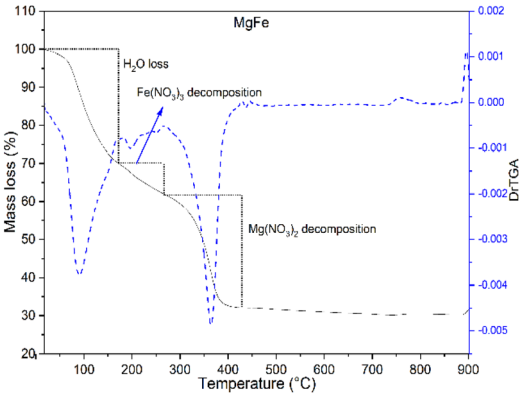

Fig. 1 Thermal deconposition curve and DTG for MgFe at air (50 mL min^{-1}) and heating rate 10 °C min^{-1}.

$Fe(NO_3)_3 \cdot 9H_2O$ and water loss. The third event occurs between 270 and 430 °C, with a loss of 29.9% by mass, attributed to the decomposition of dehydrated magnesium nitrate ($Mg(NO_3)_2$) into magnesium oxide (MgO).

Slight variations in decomposition temperatures and water loss may occur due to the mixing of the two precursors and their interactions. Additionally, since they were solubilised and dried before TG analysis, the crystal structure might have been modified. As the MgFe material is a mixture of nitrates of the respective metals, the formation of the $MgFe_2O_4$ phase can occur during heat treatment. The nitrates can decompose to form magnesium oxide and iron oxide, and the heat treatment can lead to a solid-state reaction that forms magnesium ferrite. To ensure that the thermal energy was sufficient not only for decomposition but also to promote the complete crystallisation of the $MgFe_2O_4$ (spinel) phase, temperatures of 700 °C and 900 °C were selected. The choice of 700 °C is strategically above the decomposition endpoint, avoiding the potential formation of undesirable intermediate or oxide phases that could preferentially form at 500 °C (*e.g.*, hematite, magnesium oxide), thereby impairing the material's performance and stability in contact with water. Calcination at 900 °C was performed to compare the effects of temperature on crystallite growth and crystallinity, as detailed in the X-ray Diffraction (XRD) results. This comparison allowed us to define the ideal processing window that balances high crystallinity with the lowest energy expenditure. A proposed decomposition pathway of the precursor materials and formation of magnesium ferrite is shown in eqn (1).

$$Mg(NO_3)_2 \cdot 4H_2O_{(s)} + 2Fe(NO_3)_3 \cdot 9H_2O_{(s)} \rightarrow MgFe_2O_{4(s)} + 22H_2O_{(g)} + 8NO_{2(g)} + 2O_{2(g)} \quad (1)$$

At the end of the analysis, approximately 31.2% of the material remained. This value is close to the value calculated according to eqn (1) (30.3%) if only magnesium ferrite ($MgFe_2O_4$) was formed. The results confirm that temperatures above 400 °C can alter the chemical composition of the precursor materials present in the sample, forming new structures.

X-ray diffraction (XRD)

The adsorbent materials produced were characterised by X-ray diffraction (XRD) to evaluate the effect of temperature on the formation of the Fe and Mg oxide phases (Fig. 2). Analysing the set of diffractograms, it is possible to observe peaks related to magnesium nitrate $Mg(NO_3)_2 \cdot 4H_2O$ (COD – 9011207) for the MgFe sample, consistent with the data obtained by TG, where the complete decomposition of magnesium nitrate is not observed at temperatures below 100 °C. The iron nitrate phase ($Fe(NO_3)_3$) was not identified, possibly due to the decomposition of part of the reagent used or due to the formation of an amorphous material, where $Fe(NO_3)_3$ did not recrystallise. For the sample calcined at 300 °C (MgFe300), the phase related to the magnesium nitrate precursor can still be identified. After calcination at 700 °C and 900 °C for 1 h, the samples exhibit well-defined diffraction patterns. Phases related to magnesium oxide, MgO (COD – 1000053), were found due to the excess of magnesium used in the synthesis of iron for the formation of ferrite. For all synthesised samples, the hematite α-Fe_2O_3 phase (COD – 04-003-2900) was found. It is possible to observe that with the increase in the calcination temperature (700 and 900 °C), the characteristic hematite peaks become less evident. Magnesium ferrite, $MgFe_2O_4$ (COD – 9001458), in a cubic crystal structure, organised in the inverted spinel structure and space group 227, can be observed after heat treatment at 700 and 900 °C. The results confirm the effectiveness of our strategy in using information from the literature (minimum of 600 °C) and TG to select temperatures that guarantee obtaining the desired ferrite with a synthesis route of lower environmental impact.

As the calcination temperature increases, finer and better-defined peaks for the identified ferrite phase become observable, indicating the formation of a more crystalline material. The increase in calcination temperature also increases the average crystallite size of the magnesium ferrite phase ($MgFe_2O_4$), as calculated using the Scherrer equation for the MgFe700 sample (50 nm) and the MgFe900 sample (114 nm). Finer peaks are observed for the MgFe900 sample. This result, together with the increase in crystallite size, indicates that more crystalline material is formed during the heat treatment.[46] In contrast, the heat treatment leads to a decrease in the lattice parameter observed with 8.420 Å for MgFe700 and 8.371 Å for MgFe900. These values are close to those previously reported in the literature.[47,48]

Mössbauer spectroscopy

Mössbauer spectroscopy analysis was performed at a low temperature (23 K) to enhance the spectral resolution and provide a more precise definition of the hyperfine parameters. This analysis condition indicates the formation of a ferrite with smaller particles and superparamagnetic properties (Fig. 3, 4, and Table S1 in the SI). The spectra obtained for the synthesised samples exhibit sextets characteristic of hematite (α-Fe_2O_3), which are observed for all materials (Fig. 3). The relative spectral area to this phase decreases as the calcination temperature increases, with its highest value at 74% for the MgFe300 sample and the lowest at 38% for MgFe900 (Fig. 4 and Table S1). This behaviour was also observed in the XRD, with less evident peaks for hematite. Sextets related to dispersed Fe^{3+} are observed for the MgFe (40%) and MgFe300 (26%) samples. As the calcination temperature increases, the area related to the dispersed Fe^{3+} phase decreases. For samples calcined at 700 and 900 °C for 1 h, sextets associated with this phase are no longer observed (Fig. 3 and Table S1). The Mössbauer spectroscopy results confirm the formation of ferrite ($MgFe_2O_4$) through the formation of sextets in heat treatments of 700 and 900 °C. In the cubic crystalline structure of ferrites, the oxygen atoms are arranged to form octahedral (octa) and tetrahedral (tetra) sites. The Fe^{3+} atoms preferentially occupy octahedral sites, while M^{2+} cations occupy tetrahedral sites.

Magnesium ferrite has the characteristic of organising itself with the inversion of these sites. That is, Fe^{3+} atoms can occupy tetrahedral sites while Mg^{2+} cations start to occupy octahedral sites. This configuration is also known as inverted spinel.[48,49]

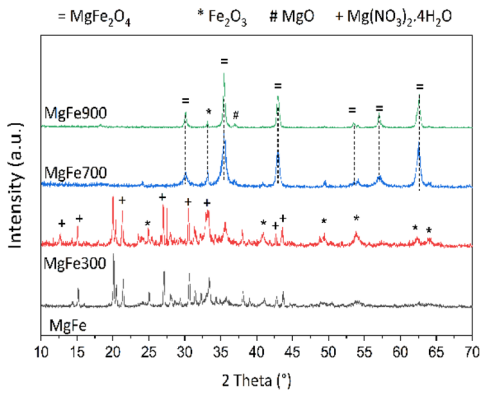

Fig. 2 X-ray diffraction for samples MgFe, MgFe300, MgFe700, and MgFe900 before and after annealing at 300, 700, and 900 °C for 1 h.

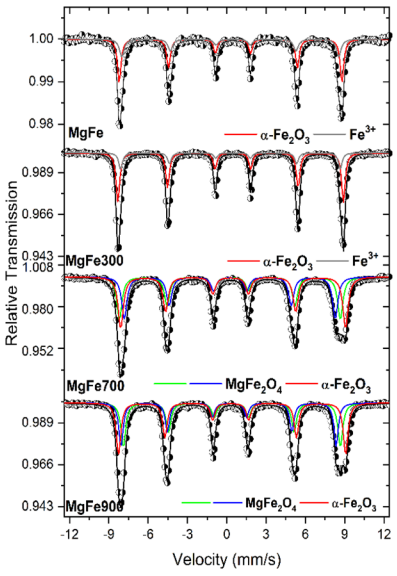

Fig. 3 Mössbauer spectra at 23 K of the adsorbent materials MgFe, MgFe300, MgFe700, and MgFe900.

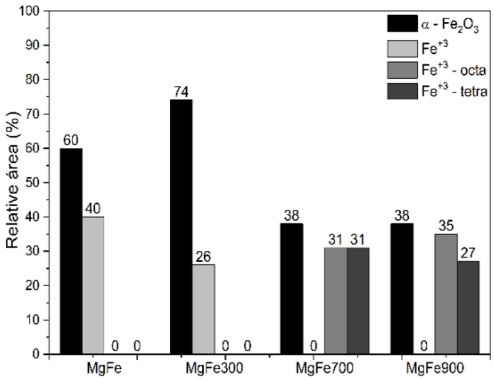

Fig. 4 Relative areas for the iron phases present in the samples MgFe, MgFe300, MgFe700, and MgFe900 obtained by Mössbauer Spectroscopy.

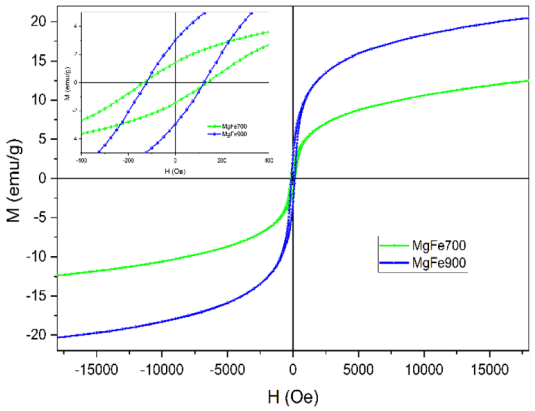

Fig. 6 Magnetisation curves obtained at room temperature for samples MgFe700 and MgFe900.

For the MgFe700 sample, the Fe^{3+} atoms of the ferrite phase ($MgFe_2O_4$) are equally distributed in the tetra and octa sites since the relative area for the tetra and octa sites is equal (31% each), indicating that the magnesium ferrite is organised in the inverted spinel structure (Fig. 3, 4, and Table S1).[50] For the MgFe900 sample, Fe^{3+} (octahedral) is observed occupying 35% of the sites, and Fe^{3+} (tetrahedral) 27%. In the latter case, the calcination temperature used can affect the crystallisation process of the materials and the rearrangement of the ions present. Thus, after calcination at 900 °C, a mixed structure between common spinel and inverted spinel can be observed for magnesium ferrite.[48,49]

Vibrating sample magnetometer (VSM)

The magnetic properties of ferrites are of great interest in a wide range of applications. The samples calcined at 700 and 900 °C for 1 h exhibited a strong interaction capacity with magnets (Fig. 5). VSM characterised the materials MgFe700 and MgFe900 to determine their magnetic properties (Fig. 6 and S1). The hysteresis curves show an 'S' shape, indicating a soft magnetisation characteristic in the samples (Fig. 6). The magnetic saturation (M_s) values increase with the calcination temperature, with values of 12.54 emu g^{-1} for MgFe700 and 20.43 emu g^{-1} for MgFe900 (Table 2). The increase in the calcination temperature of the materials can cause the migration of Fe^{3+} cations from tetrahedral sites to octahedral sites, facilitating the better accommodation of Mg^{2+} ions in these sites and forming a mixed spinel structure, as observed by Mössbauer spectroscopy, which leads to changes in the M_s values. This migration can occur due to the difference in radius of the Mg^{2+} (0.720 nm) and Fe^{2+} (0.645 nm) cations.[48,49]

The residual magnetisation (M_r) values also increase with the calcination temperature, from MgFe700 (1.69 emu g^{-1}) to MgFe900 (3.24 emu g^{-1}).[47] The low values of the M_r/M_s ratio indicate a superparamagnetic character of the analysed samples, as indicated by Mössbauer spectroscopy (Table 2). The narrow shape of the hysteresis curve in Fig. 6 reinforces this information, evidencing that a considerable part of the particles is superparamagnetic (Fig. 6).[47,48] The narrow shape also indicates low coercivity (H_c), with values of 29.63 Oe for MgFe700 and 16.78 Oe for MgFe900. The low H_c values suggest that the material can be demagnetised for potential electronic applications. The magnetic property values for the MgFe700 and MgFe900 samples obtained from the hysteresis curve are graphically represented in the SI (Fig. S1).

Since the material presents significant magnetic activity, its recovery in an aqueous medium becomes more efficient for applications in contaminant removal. The values of M_s, M_r, M_r/M_s, H_c and the shapes of the VSM curves are like those found for magnesium ferrites previously synthesised in other works.[20,47–49]

Fig. 5 Interaction of MgFe700 sample with neodymium magnet.

Scanning electron microscope (SEM) and energy dispersive spectroscopy (EDS)

The samples' morphology was examined using Scanning electron microscopy (SEM – Fig. 7), and Energy dispersive spectroscopy (EDS), as shown in Fig. S2 of the SI. It was found that the increase in temperature contributed to the formation of a rougher surface, in addition to providing the formation of agglomerates for the samples calcined at 700 and 900 °C, due to

Table 2 Magnetic properties for samples MgFe700 and MgFe900

Sample	M_s (emu g^{-1})	M_r (emu g^{-1})	M_r/M_s	H_c (Oe)
MgFe700	12.54	1.690	0.1347	29.630
MgFe900	20.43	3.245	0.1588	16.782

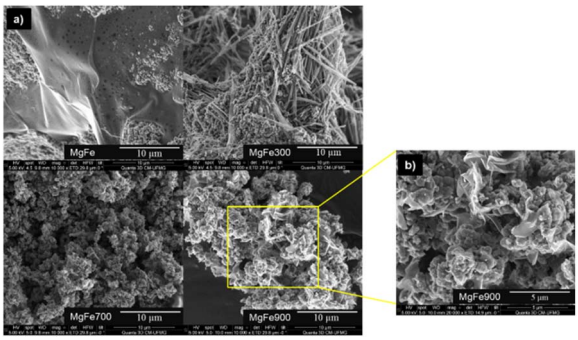

Fig. 7 (a) Micrographs of samples MgFe, MgFe300, MgFe700 and MgFe900 at 10 000× magnification; (b) magnification of the highlighted region for sample MgFe900 at 20 000×.

the magnetic characteristic that materials with the presence of magnesium ferrite have (Fig. 5 and 6).

The MgFe sample exhibits smoother areas with encrusted lumps, indicating the initial stages of material decomposition. When treated at 300 °C, sample MgFe300 forms acicular structures, and small clusters of particles can be observed, possibly related to the decomposition processes of the precursors. From the treatments at 700 and 900 °C, a rougher surface is observed, composed of many agglomerates with more uniform and similar particles. The MgFe700 sample presents a surface with grooves, which may have been formed by the release of gases in the decomposition of the precursor nitrates. Agglomerates and grooves are also present for the MgFe900 sample, in addition to the formation of thin petal-shaped sheets, which are highlighted in Fig. 7(b). The magnetic characteristics of materials may favour the observed agglomerates, particularly in the presence of magnesium ferrite, as described in Mössbauer and VSM analyses. The spectra obtained by EDS for the MgFe700 and MgFe900 samples, shown in the SI (Fig. S2), allow the evaluation of the predominant composition and distribution of the elements in the obtained samples. The spectra indicate peaks related to magnesium (Mg), iron (Fe) and oxygen (O).

Determination of the adsorption capacity of PO_4^{3-}

The synthesised materials were subjected to phosphate adsorption tests in water. A slight trend of increasing adsorption capacity with increasing calcination temperature is observed (Fig. S3). The MgFe and MgFe300 samples demonstrated phosphate removal efficiency, with adsorption capacities of 11.4 mg g^{-1} and 13.5 mg g^{-1}, respectively. The adsorption capacity for these materials can be correlated with the presence of hematite in the samples, as evidenced by XRD and Mössbauer spectroscopy analyses. Hematite has phosphate removal capacity, as shown in previous works.[51,52] There is no indication of phosphate precipitation due to reaction with Mg^{2+} and Fe^{3+} ions since the atomic absorption analysis does not show the presence of these soluble cations significantly after washing the material, MgFe (Mg^{2+} < 0.02 mg L^{-1} and Fe^{3+} < 0.08 mg L^{-1}) and MgFe300 (Mg^{2+} 0.38 mg L^{-1} and Fe^{3+} < 0.08 mg L^{-1}), as shown in the SI (Fig. S4 and S5).

The MgFe700 and MgFe900 samples showed an increase in the PO_4^{3-} removal capacity: 16.8 mg g^{-1} and 19.7 mg g^{-1}, respectively (Fig. S3). For these samples, Mg and Fe are retained in magnesium ferrite and hematite structures, indicated by XRD and Mössbauer spectroscopy. Magnesium is more leached than iron during washing, with atomic absorption measured Mg^{2+} (2.7 mg L^{-1}) and Fe^{3+} (<0.08 mg L^{-1}) for MgFe700 and Mg^{2+} (7.6 mg L^{-1}) and Fe^{3+} (<0.08 mg L^{-1}) for MgFe900, after four washes in both cases. The increase in the phosphate adsorption capacity may be related to the presence of magnesium ferrite in the samples. Another factor that may influence the adsorption process is the surface area. MgFe700 and MgFe900 samples show a surface area equal to 8.9 and 7.8 m^2 g^{-1}, respectively (Fig. S6). The N_2 adsorption/desorption curve profile can be classified as a type II isotherm according to the IUPAC description,[53] which is defined for non-porous or macroporous materials. The SEM images show that nanoparticles were not formed, which corroborates the low surface area of the samples. These factors may enhance the presence of magnesium ferrites in MgFe700 and MgFe900, thereby contributing to phosphate removal.

Infrared (IR) spectroscopy can help indicate the presence of surface functional groups after the adsorption of the materials. Therefore, the MgFe700 and MgFe900 samples were subjected to IR analysis before and after adsorption (Fig. S7). OH bands close to 3360–3370 cm^{-1} were observed, attributed to OH stretching of hydroxyl groups on the surface of the material or water on the surface, mainly for the samples after adsorption (MgFe700P and MgFe900P). The presence of OH groups may be linked to the hydration of Fe and Mg on the surface of the material. The bands close to 519–523 cm^{-1} can be attributed to the stretching of tetrahedral Fe–O bonding sites.[54] It was not possible to observe bands related to octahedral sites due to the device's limitation, which resulted in regions below 500 cm^{-1} being poorly defined. Therefore, bands of octahedral sites were not identified. A new band is observed after phosphate adsorption, appearing at approximately 1033–1046 cm^{-1}, and can be attributed to the P–O bond.[55] This result reinforces the adsorption of phosphate on the surface of the MgFe700 and MgFe900 samples.

Adsorption tests at different pH levels, pH_{PZC} determination, and competition tests were conducted on the two materials containing the ferrite phase, MgFe700 and MgFe900, to evaluate their phosphate adsorption capacity under various conditions. Subsequently, adsorption and desorption tests were performed to assess the reuse potential of these materials.

Phosphate adsorption isotherm studies for magnesium ferrites

The isotherm tests studied the adsorption behaviour of MgFe700 and MgFe900 materials against different initial concentrations of PO_4^{3-} (C_i – 10–250 mg L^{-1}; Fig. 8 and 9). The data obtained show that the amount of phosphate removed increases as the initial concentration of the PO_4^{3-} ion increases.

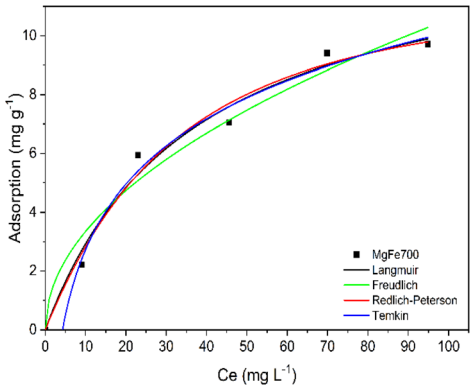

Fig. 8 Phosphate adsorption isotherm for sample MgFe700 ($[PO_4^{3-}]$ C_i – 10–250 mg L^{-1}, adsorbent dose: 1 g L^{-1}, 150 rpm, 24 h, 298 ± 0.1 K).

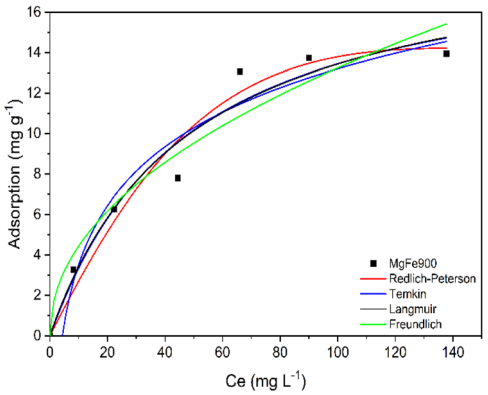

Fig. 9 Phosphate adsorption isotherm for sample MgFe900 ($[PO_4^{3-}]$ C_i – 10–250 mg L^{-1}, adsorbent dose: 1 g L^{-1}, 150 rpm, 24 h, 298 ± 0.1 K).

The isothermal study evaluated the adsorption behaviour using four models: Langmuir, Freundlich, and Temkin models, which use two parameters to explain the interaction between the adsorbent and adsorbate, and the Redlich–Peterson model, which uses three parameters. The R^2 value was used to analyse the fit of the isotherm models to the experimental data (Table 3), and the parameters of each model were calculated according to the equations presented in the SI (Table S2).[56–60]

The phosphate adsorption isotherm results for the MgFe700 sample show a better fit to the Temkin model with R^2 0.985 (Fig. 8). This model accounts for indirect interactions between the adsorbent and adsorbate, assuming the adsorption heat (ΔH_{ads}) of all molecules decreases linearly as the adsorption layer forms. The Temkin equation does not account for high and low values of adsorbate concentration.

Therefore, it is only valid for medium ranges of ion concentrations used.[56–60] The effectiveness of the Temkin isotherm model in describing phosphate adsorption on MgFe700 is attributed to the surface heterogeneity of the material. The Mg and Fe atoms in the material can function as phosphate adsorption sites. Because they have different

Table 3 Isotherm parameters calculated for the different models applied to the materials MgFe700 and MgFe900

		Sample	
Isoterm model	Parameter	MgFe700	MgFe900
Langmuir	K_L	0.037	0.020
	q_{max}	13.72	19.93
	R^2	0.9805	0.9548
Freundlich	n	2.0060	2.1044
	K_F	1.0628	1.4852
	R^2	0.9610	0.9322
Temkin	A	0.2343	0.2305
	B	3.2057	4.2086
	R^2	0.9856	0.9431
Redlich–Peterson	K_R	0.3325	0.2763
	a_R	0.0127	6.0431×10^{-4}
	n	0.883	0.588
	R^2	0.9749	0.9499

binding energies, this indicates a more heterogeneous adsorption between these different adsorption sites. The data also present a good fit to the Langmuir isotherm model, R^2 0.980 (Table 3). This model calculates a maximum adsorption of q_{max} = 13.7 mg g^{-1}, indicating the formation of a monolayer of adsorbate on magnesium ferrite.

The isotherm curve obtained from the experimental data for the MgFe900 material shows the best fit for the Langmuir model, with $R^2 = 0.959$, and a calculated maximum adsorption value of $q_{max} = 19.93$ mg g^{-1} (Fig. 9 and Table 3). The Langmuir model is empirical and based on the premise that all adsorption sites are uniform and equally available to all adsorbate particles in the solution. Therefore, no interaction between adsorbates is in adjacent sites, and all adsorbate molecules adhere to the adsorption sites with the same energy.[57,58,60–62] The Temkin model also shows a good fit (R^2 = 0.913) for the MgFe900 sample, indicating heterogeneity in the adsorption of the material surface (Table 3). Scanning electron microscopy images do not reveal significant changes in the surface morphology of the material after calcination at 900 °C for one hour, compared to MgFe700. The N_2 adsorption/desorption isotherms also do not indicate surface modifications. The relative areas of Fe^{3+}, determined by Mössbauer spectroscopy, remain practically unchanged compared to the MgFe700 sample. These results suggest that the surface of the material does not undergo substantial changes with variations in the calcination temperature, indicating that the adsorption sites remain constant. Consequently, the MgFe900 sample may exhibit an adsorption mechanism characterised by the formation of a monolayer and maintains a specific heterogeneity since Mg and Fe can act as adsorption sites of PO_4^{3-}.

Kinetic studies of phosphate adsorption onto magnesium ferrites

The phosphate removal over time for the MgFe700 and MgFe900 materials was determined from the adsorption kinetics from a PO_4^{3-} solution of concentration 50 mg g^{-1}, at

25 °C (Fig. 10 and 11). These results are crucial for a better understanding of the adsorption process in various applications. The kinetic curve for the MgFe700 material indicates that the adsorption capacity increases with increasing contact time (Fig. 10). The process of adsorption can be delineated into two distinct phases. The first stage is fast, occurring 240 min before, and this event may be related to the diffusion of PO_4^{3-} ions on the surface of the material. The second event has a controlled rate and occurs after 240 min, and it may be related to intra-particle diffusion.[25] After 540 min, the adsorption curve shows stability, indicating that the material no longer adsorbs phosphate after this time. MgFe900 exhibits a result similar to that of the MgFe700 sample, with two main stages controlling the reaction (Fig. 11). The first stage is more accelerated and occurs within the first 90 minutes. The second stage begins after 90 minutes and continues for up to 360 min until stability is reached. This result shows that the MgFe900 material reaches adsorption equilibrium after 6 h of contact with the phosphate solution.

Three kinetic models were used to analyse the experimental data and understand the adsorption mechanism: the pseudo-first-order, pseudo-second order, and Elovich models. The kinetic parameters for phosphate adsorption on the surfaces of MgFe700 and MgFe900 materials were calculated (Table 4). The R^2 parameter was used to evaluate the models' fit to the experimental data, and the equations used are provided in the SI (Table S2).[63–66] The adsorption curves of the materials show better fits to the Elovich kinetic model. MgFe700 material presented a coefficient of determination (R^2) of 0.942, and the MgFe900 presented an R^2 of 0.894. The maximum adsorption capacity values achieved were 9.5 mg g^{-1} for MgFe700 and 8.5 mg g^{-1} for MgFe900. The Elovich model is quite helpful for evaluating chemical adsorption, indicating that adsorption occurs only at localised sites and that interactions between ions sorbed into the material occur.[64,66] The best fit to the Elovich model reflects the adsorption process, which is influenced by two aspects: heterogeneity and the energy barrier (E_a). The E_a cannot be measured because we only experimented with one temperature; however, the parameters α (initial rate) and β (coverage factor) are intrinsically linked to this barrier. The observation that MgFe900 has a larger α (0.667) than Mg700 (0.394), and reaches equilibrium more quickly (360 min), suggests that, for this material, the activation energy barrier can be more readily overcome at the initial sites, resulting in faster kinetics, even though MgFe700 reaches a slightly higher maximum capacity. The parameter β is related to the increase in activation energy with increasing surface coverage. The value of beta for MgFe900 (0.728) is slightly higher than that for MgFe700 (0.648). A higher beta value implies that the adsorption activation energy increases more rapidly as the MgFe900 surface becomes more fully covered. This is consistent with the rapid equilibrium reached for this material, suggesting that saturation of active sites occurs more sharply. The strong fit to the Elovich model confirms that phosphate sorption is controlled by a chemisorption mechanism. The results indicate that the cations Mg^{2+} and Fe^{3+} serve as active sites for PO_4^{3-} sorption. The strong interaction of Mg with the phosphate ion, due to its small ionic radius,[25] suggests that inner-sphere complexation is primarily responsible for adsorption, in line with previous studies on metal oxides and magnesium-containing adsorbents. The inner-sphere complexation mechanism may be primarily responsible for the adsorption of

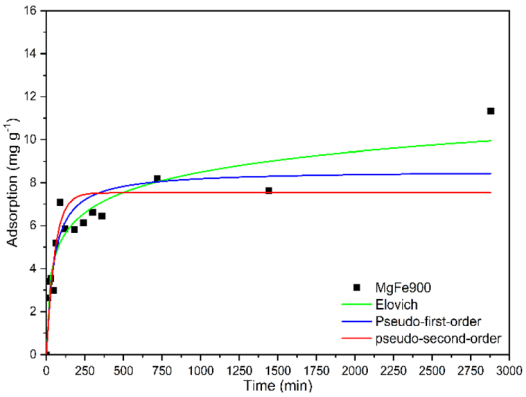

Fig. 11 Adsorbed phosphate amount *versus* contact time for MgFe900 ($[PO_4^{3-}] = 50$ mg g^{-1}, adsorbent dosage: 1 g L^{-1}, 150 rpm, 298 ± 1 K).

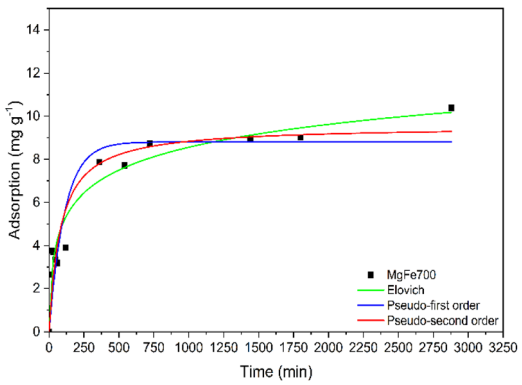

Fig. 10 Adsorbed phosphate amount *versus* contact time for MgFe700 ($[PO_4^{3-}] = 50$ mg g^{-1}, adsorbent dosage: 1 g L^{-1}, 150 rpm, 298 ± 1 K).

Table 4 Parameters of kinetic models for phosphate adsorption onto magnesium ferrite MgFe700 and MgFe900

		Sample	
Kinetic model	Parameter	MgFe700	MgFe900
Pseudo-first order	k	0.008	0.018
	q_e	8.80	7.53
	R^2	0.830	0.719
Pseudo-second order	k_2	0.001	0.002
	q_e	9.54	8.57
	R^2	0.888	0.806
Elovich	α	0.394	0.667
	β	0.648	0.728
	R^2	0.942	0.894

phosphate by metal oxides.[5,25] The interaction between phosphate and sediments, as well as soils, has been previously examined employing the Elovich model. Materials containing magnesium have been used to remove phosphate from water with adsorption mechanisms consistent with the results obtained in this work.[64,65,67,68]

Study of the influence of initial pH on adsorption capacity

The pH of the solution strongly influences the adsorption capacity of the materials.[4,28,69] First, by altering the distribution of the phosphate species present in the medium and second, by modifying the surface charge of the materials. The initial pH's impact on phosphate adsorption by magnesium ferrites was studied over a pH range of 3 to 10 (Fig. 12). The materials show a tendency to decrease their adsorption capacity at high pH values. At pH 7, the MgFe700 sample achieved the best adsorption capacity of 28.6 mg g^{-1}, whereas the MgFe900 sample showed its highest adsorption at pH 5, with a capacity of 24.3 mg g^{-1} (Fig. 12). The results in the pH range of 3 to 7 are favourable for PO_4^{3-} removal. High pH conditions are not ideal for phosphate removal. These results indicate that magnesium ferrite-based adsorbent materials can be utilised over a wide pH range, enabling their application to various effluents. The pH_{PZC} values for MgFe700 and MgFe900 were determined to assess the effect of pH on the material's surface charge distribution. The pH_{PZC} values for MgFe700 and MgFe900 were 8.5 and 8.7, respectively (SI S8). A similar outcome was noted for mesoporous graphene oxide–ferrite nanocomposites, with a zero charge point value of 8.5. For both adsorbent materials evaluated, at pH levels below 8.5, adsorption remained high, whereas above this zero-charge point, phosphate adsorption decreased considerably.[70] The efficiency of phosphate removal at lower pH values is due to an increase in the adsorbent's positive charge, which favours the adsorption of anions. Under basic conditions with higher OH^- concentrations, the material's surface charge is predominantly negative, favouring cation adsorption. The pH of the medium affects the distribution of phosphate species and impacts the adsorption process. This process includes electrostatic attraction between the oxyanion and protonated hydroxyl groups, as well as ligand exchange. At pH levels lower than pH_{PZC}, the surface of the material becomes positively charged, which can contribute to the electrostatic interaction between the adsorption sites on the surface of the adsorbent and the anionic adsorbate. Conversely, under more basic conditions, the electrostatic interactions are disfavored, and the adsorption capacity decreases. The metals Mg and Fe also interact significantly with OH^- ions, which, under basic conditions, can compete with PO_4^{3-} for adsorptive sites on the surface of the materials. Therefore, the net negative surface charge on the adsorbent surface and competition between OH^- and PO_4^{3-} ions for adsorption sites can contribute to a decrease in the amount of adsorbed phosphate ions.

To investigate the contribution of secondary mechanisms, the stability of the materials was evaluated by measuring Mg and Fe leaching in the presence of phosphate at pH 3, 5, and 7 (SI S9 and S10). The results demonstrated excellent stability of the matrix, as the Fe lixiviated concentration was consistently very low and near the detection limit (*e.g.*, 0.08 mg L^{-1} at pH 3 for MgFe700), even in acidic media. However, significant Mg lixiviation was observed, particularly under acidic conditions. For example, at pH 3, MgFe700 lixiviated 26.23 mg L^{-1} of Mg, and MgFe900 lixiviated 33.23 mg L^{-1} of Mg. This Mg dissolution suggests a pH-dependent dual removal mechanism: under strongly acidic conditions (pH 3), Mg lixiviation is dominant, and subsequent chemical precipitation (*e.g.*, $Mg(H_2PO_4)_2$ formation) may become the dominant mechanism. Conversely, at pH 7, Mg lixiviation is minimal (*e.g.*, 7.78 mg L^{-1} for MgFe900), confirming that surface adsorption (activated chemisorption) remains the primary mechanism. The results from the pH experiments (with $q_{max} = 28.6$ mg g^{-1} and 24.3 mg g^{-1}) represent the material's actual maximum capacity under ideal conditions. The isotherm results (13.7 mg g^{-1} and 19.9 mg g^{-1}) are more representative of natural waters used in applications, where pH varies widely and is uncontrolled, resulting in an underestimation of the material's maximum potential capacity.

The phosphate adsorption mechanism scheme proposed (Fig. 13), highlighting three steps: step 1 – hydration, which represents the interaction of water molecules with the material

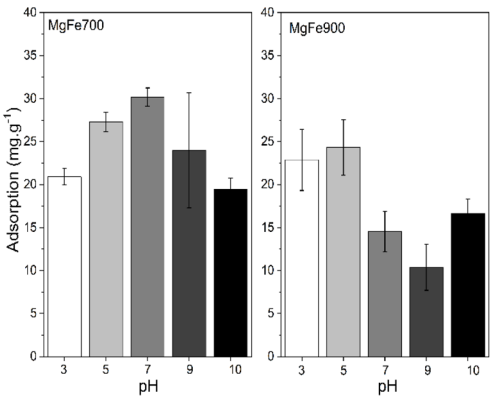

Fig. 12 Phosphate adsorption capacity of MgFe700 and MgFe900 materials at different pH (adsorbent dose: 1 g L^{-1}, [PO_4^{3-}] 50 mg g^{-1}, 24 h, 150 rpm).

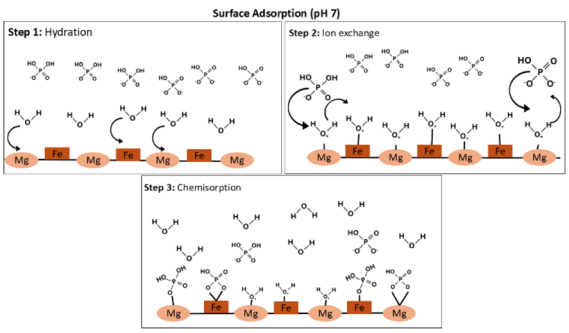

Fig. 13 Scheme of the phosphate removal mechanism by magnesium ferrite ($MgFe_2O_4$), highlighting chemisorption at pH7 through distinct sites.

surface; step 2 – ion exchange, which shows the replacement of water molecules on the ferrite surface by phosphate species ($H_2PO_4^-$/HPO_4^{2-} – pH 7) present in the solution; step 3 – which shows the phosphate species adsorbed by Mg and Fe ions through an innersphere bond or chemisorption.

Anion competition assays

In natural waters, a complex mixture of ions is present that can influence the adsorption capacity of ions of interest. MgFe700 and MgFe900 were evaluated as phosphate adsorbents in the presence of Cl^-, SO_4^{2-}, NO_3^-, HCO_3^-, and CO_3^{2-} (Fig. 14). For the MgFe700 sample, the presence of HCO_3^- and SO_4^{2-} reduces the phosphate removal capacity by 11% to 15%, respectively. Competing ions, such as Cl^- (17%) and NO_3^- (18%), can increase the phosphate removal capacity of the material, whereas the presence of CO_3^{2-} (3%) does not significantly alter the phosphate adsorption capacity. For the MgFe900 sample, the adsorption test performed in the presence of Cl^- (9%), NO_3^- (26%), and CO_3^{2-} (26%) contributes to increasing the PO_4^{3-} removal capacity. The presence of SO_4^{2-} (1%) and HCO_3^- (−32%) decreases the phosphate capture capacity of the material. The influence of SO_4^{2-} and CO_3^{2-} ions on the adsorption process remains unclear. Competing ions can alter the ionic strength or change the pH values of the reaction medium, and these factors can influence the adsorption capacity of the materials. Phosphate adsorption on oxides can follow adsorption on specific sites, while ions such as Cl^- and NO_3^- can undergo nonspecific adsorption and, therefore, do not compete for adsorption sites with PO_4.[3–5]

The decrease in the adsorption capacity of the materials due to HCO_3^- may be attributed to the rise in the pH of the solution and the competition for adsorption sites between PO_4^{3-} and HCO_3^- ions. The initial pH of the PO_4^{3-}/HCO_3^- solution is close to 8.3, and at the end of adsorption, close to pH 9. For the MgFe700 sample, the influence of pH is negligible. Therefore, there is a minor reduction in the adsorption capacity of PO_4^{3-} (1%). The MgFe900 material is affected by pH (Fig. 14). Therefore, there is a greater reduction in the phosphate adsorption capacity in the presence of bicarbonate (−32%). The decrease in the phosphate adsorption capacity in the presence of bicarbonate also indicates competition between the adsorption sites of the material.

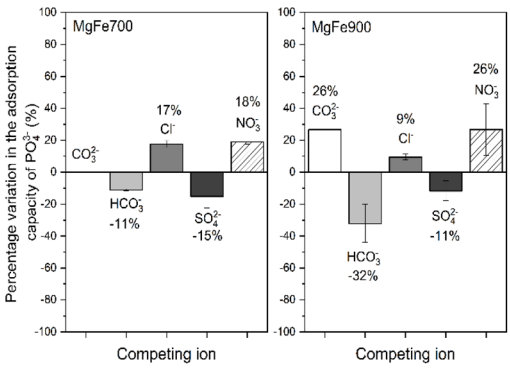

Fig. 14 Percentage variation of phosphate adsorption in the presence of competing ions (adsorbent dose: 1 g L^{-1}, PO_4^{3-}/ion concentration = 50 mg g^{-1}, 24 h, 150 rpm).

Phosphate desorption assay

Stable, reusable adsorbents for successive adsorption–desorption cycles are crucial for a more cost-effective, sustainable process. Adsorption–desorption tests were conducted to assess the reusability of the synthesised phosphate adsorbents. Adsorption tests at different pH levels showed that the adsorption capacity decreases with increasing pH. This result indicates that basic conditions above the pH_{PZC} values can favour desorption. Other studies have yielded similar results and employed NaOH solutions in the desorption step.[30] Therefore, two NaOH concentrations were used to assess phosphate release: NaOH 0.5 mol per L (NaOH 1) and NaOH 1 mol per L (NaOH 2). Different ionic strengths can also influence the removal and release of phosphorus in water.[71] Consequently, this study examined two ionic strength conditions using KCl solutions, 0.01 mol per L (KCl 1) and 0.1 mol per L (KCl 2).

Desorption results for the four different conditions were initially evaluated (SI S11). Under basic conditions, the first desorption step of the MgFe700 material exhibited a phosphate release capacity of 11 mg g^{-1} for 0.5 mol per L NaOH (NaOH 1) and 15.3 mg g^{-1} for 1 mol per L NaOH (NaOH 2). Using a KCl solution, the material desorbed 4 mg g^{-1} for 0.01 mol per L (KCl 1) and 6 mg g^{-1} for 0.1 mol per L (KCl 2). For the MgFe900 material, the basic conditions removed 15 mg g^{-1} and 11 mg g^{-1}, respectively, for NaOH solutions of 0.5 mol per L (NaOH 1) and 1 mol per L (NaOH 2). Using a KCl solution, 4 mg g^{-1} was desorbed with 0.01 mol per L (KCl 1) and 6 mg g^{-1} with 0.1 mol per L (KCl 2). The application of KCl solutions at concentrations of 0.01 mol per L (KCl 1) and 0.1 mol per L (KCl 2) resulted in the release of 4 mg g^{-1} and 7 mg g^{-1} of MgFe900 material, respectively (S11).

The alkaline conditions showed better phosphate desorption capacity for both materials. In alkaline media, electrostatic repulsions can increase, as previously discussed, leading to phosphate desorption from the material surface.[30,72] For the MgFe700 sample, the 1 mol per L NaOH condition yielded higher phosphate desorption efficiency. To avoid using highly alkaline conditions, a 0.5 mol per L NaOH solution was chosen for reuse tests of both materials. Changing the ionic strength can alter the charge distribution at the material surface and, consequently, modify phosphate dynamics between the surface and the solution.[71] The phosphate desorption capacity decreases when KCl solutions of varying concentrations are applied. Phosphate desorption by saline solutions is more efficient when physical adsorption occurs on the surface of the material.[30,72] As previously discussed, the kinetic and isotherm data indicate chemical adsorption occurring on the surface of the adsorbent materials studied in this work. Therefore, a desorption process with KCl may not be efficient for recovering the previously removed phosphorus. Still, the more

concentrated KCl solution showed better phosphate release, and 0.1 mol per L KCl was used for the reuse tests.

The reusability of the synthesised materials was evaluated by repeating the adsorption–desorption cycle four times with the extracting solutions of 0.5 mol per L NaOH (Fig. 15A and B) and 0.1 mol per L KCl (Fig. 15C and D). The adsorption capacity decreases with the number of reuse cycles, considering the mass of PO_4^{3-} contained in 15 mL of the 50 mg per L solution. The MgFe700 material exhibits a reduction in the removal capacity of PO_4^{3-} over the cycles, with a decrease from 26% (14.2 mg g^{-1}) in the first cycle to 1% (0.5 mg g^{-1}) in the 4th cycle when the 0.1 mol per L KCl solution was applied. Using the 0.5 mol per L NaOH solution, the MgFe700 material presents a 3% (1.7 mg g^{-1}) removal in the 3rd cycle and does not show a significant phosphate removal capacity after four cycles. The MgFe900 material also presents a reduction in phosphate removal capacity throughout the cycles. When desorbed with 0.1 mol per L KCl, the removal percentage drops from 19% (13.1 mg g^{-1}) in the first cycle to 3% (1.5 mg g^{-1}) in the third cycle, and no removal is observed in the 4th cycle of application of the material. When NaOH is used as the desorbent solution, the material also shows a decrease in adsorption capacity across successive cycles. The PO_4^{3-} removal percentage drops from 19% in the 1st cycle to 2% (1 mg g^{-1}) for the 4th cycle.

The results show that the phosphate adsorption capacity decreases with successive cycles for both desorbent solutions, and that the adsorbent materials exhibit low reusability, even after up to 3 cycles. The interaction between Mg and Fe atoms and the PO_4^{3-} ion explains this observation. This strong interaction, which can lead to chemical adsorption, hinders the release of phosphate into the solution. Chemical adsorption, with strong binding energy (K_{ps} $Mg_3(PO_4)_2$ 1.04×10^{-24} and $FePO_4 \cdot 2H_2O$ 9.91×10^{-16}), hinders the exchange of phosphate ions adhered to the surface of the material for OH^- ions. The low release of PO_4^{3-} observed is due to species physically adsorbed by the material. When NaOH and KCl solutions are introduced, an ion exchange involving PO_4^{3-} and OH^- or Cl^- may occur, facilitating the release of P from the solution. Chemical adsorption dominates, with few species being physically adsorbed or released when extractant solutions are added. Therefore, the concentration of PO_4^{3-} is low. Loss of adsorption capacity may occur due to incomplete desorption of adsorption sites or changes in the material surface caused by the application of desorbent solutions. With successive cycles, the adsorption capacity decreased significantly because adsorption sites became unavailable. Other desorption conditions can be tested in the future to evaluate the renewal of the adsorbent and recover the phosphorus. The observed low reusability (significant capacity loss after 1–2 cycles) is a direct consequence of the activated chemisorption mechanism, as indicated by the Elovich model. The strength of the bonds formed *via* inner-sphere complexation between phosphate and the Mg/Fe sites of the ferrite necessitates more aggressive regeneration conditions than those tested. To optimise reusability for purification applications, future work should focus on desorption optimisation by exploring stronger agents, such as concentrated hydroxides or chelating organic acids (*e.g.*, citric acid), by using continuous-flow systems, or heat-assisted approaches. However, this operational limitation does not limit the material's practical applicability; instead, it directs it towards a circular economy concept. The saturated adsorbent should not be viewed as waste but rather revalued as a slow-release fertiliser (SRF) for phosphate and magnesium. This application transforms the spent material into a high-value-added product, resolving the challenge of final disposal while ensuring the recovery of essential nutrients. The technical and economic feasibility of its use as an SRF in different soil types must be the focus of the next phase of research.

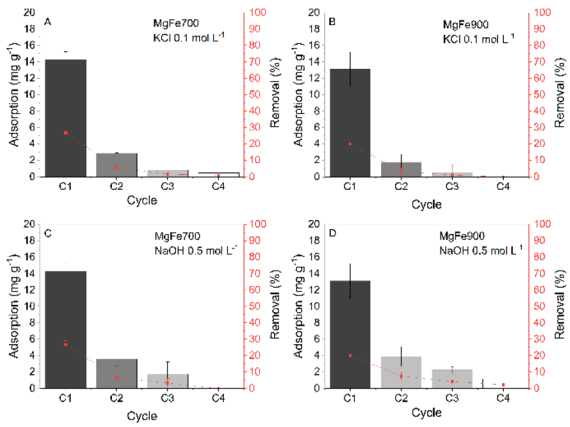

Fig. 15 Phosphate adsorption capacity (mg g^{-1}) and phosphate removal efficiency (%) after four cycles using 0.1 mol per L KCl (A and B) or 0.5 mol per L NaOH (C and D) for MgFe700 and MgFe900 adsorbents, considering the mass of PO_4^{3-} contained in 15 mL of the 50 mg L^{-1}.

A comparison between MgFe700 and MgFe900 reveals a trade-off between the energy cost of synthesis and adsorption kinetics. The synthesis of MgFe700 is favoured by its significant energy savings (MgFe700 at 700 °C *vs.* MgFe900 at 900 °C), resulting in a smaller carbon footprint in production. Although MgFe900 exhibits faster kinetics (hydraulic residence time of 360 min), the final removal capacities (q_{max} of optimal pH: 28.6 mg g^{-1} for MgFe700 and 24.3 mg g^{-1} for MgFe900) are comparable. Furthermore, the nitrate-based synthesis route, which generates NO_x, can mitigate its environmental impact by channelling and repurposing the gas for the production of diluted nitric acid, thereby increasing the overall sustainability of the process.[73] Prioritising sustainability and reducing the carbon footprint, MgFe700 is considered the optimised material, as it achieves similar efficiencies while providing a significant 200 °C energy saving in the calcination step.

The materials MgFe700 and MgFe900 presented adsorption capacities similar to or higher than those of other magnetic materials (Table 5). This shows that materials containing magnesium ferrite can be applied as adsorbents for phosphate removal in water. The materials can be recovered by magnetic separation after the sorption process, allowing for the use of more abundant and cheaper precursors for the production of adsorbents, as in the case of using Mg salt ($Mg(NO_3)_2 \cdot 6H_2O$) instead of Cu, Zr, and Mn salts.

Table 5 Maximum adsorption capacity of phosphate for different magnetic materials

Material	pH	q_e	Ref.
Manganese modified E33	7	30.9 mg g^{-1}	74
Magnetic zirconium-iron oxide	4	21.3 mg g^{-1}	75
$CuFe_2O_4$	2.34	13.5 mg g^{-1}	76
Mesoporous $NiFe_2O_4$	3	39.3 mg g^{-1}	77
MgFe700	7	28.6 mg g^{-1}	This work
MgFe900	5	24.3 mg g^{-1}	This work

Conclusions

Magnesium ferrite $MgFe_2O_4$ was synthesised with an inverted spinel structure under heating at 700 °C and mixed spinel at 900 °C. The cubic mixed spinel structure for the magnesium ferrite was confirmed by X-ray diffraction and Mössbauer spectroscopy results. VSM results indicate the formation of superparamagnetic ferrite, consistent with previously published findings. The superparamagnetic characteristic of the material shows ease of removal and recovery of the adsorbent material after application as an adsorbent in water, reducing filtration costs and material waste. The adsorption results show that the presence of $MgFe_2O_4$ contributes to a greater removal of phosphate in water, with preliminary values of 16.8 mg g^{-1} for MgFe700 and 19.7 mg g^{-1} for MgFe900. Adsorption in slightly acidic or neutral media favours phosphate removal, with values equal to 28.6 mg g^{-1} at pH 7 for MgFe700 and 24.3 mg g^{-1} at pH 5 for MgFe900. The adsorbents exhibit a significant phosphate removal capacity over a wide pH range, enabling their application in various effluents. The presence of competing ions, such as Cl^-, NO_3^-, and HCO_3^-, can influence the adsorption capacity of the MgFe700 and MgFe900 materials, thereby increasing phosphate removal rates by up to 25%. However, the presence of SO_4^{2-} and CO_3^{2-} can decrease the adsorption capacity by up to 33%. Therefore, the materials have good selectivity for phosphate adsorption since the phosphate adsorption capacity is not lost in the presence of other anions. Phosphate adsorbent material based on magnesium ferrite can be prepared at 700 °C, a condition that is energy-efficient and yields results very similar to those obtained at 900 °C. Kinetic and adsorption isotherm tests indicate that chemical adsorption occurs at specific sites. The MgFe700 and MgFe900 samples showed the best fit with the Langmuir isothermal model and Elovich kinetic model. The reuse experiments demonstrated a strong interaction between phosphate and magnesium ferrite-based materials, characterised by low desorption and material reuse rates.

Author contributions

Matheus H. P. Araújo participates in the data analysis, preparation, creation, and presentation of the published work by the original research group, specifically in critical review and revision, including pre- and post-publication stages, as well as conducting research and investigation processes, such as performing experiments and data collection. Laura M. F. Moreira conducts research and investigation processes, specifically performing experiments or collecting data and evidence, providing commentary, and revising the manuscript. José D. Ardisson performed the Mössbauer characterisation, collected the data, conducted the critical review, provided commentary, and revised the manuscript. Rochel M. Lago contributes to the leadership of research activity planning and execution, as well as critical review, commentary, and revision. Juliana C. Tristão is responsible for overseeing and leading research activity planning and execution, including mentorship external to the core team, and acting in critical review and revision – encompassing both pre- and post-publication stages.

Conflicts of interest

There are no conflicts to declare.

Data availability

The data that support the findings of this study are available from the corresponding author upon reasonable request. Raw TGA, XRD, and FTIR characterisation data are available at DOI: https://doi.org/10.57760/sciencedb.29440.

Supplementary information (SI) is available. See DOI: https://doi.org/10.1039/d5su00715a.

Acknowledgements

The Fundaçãoo de Amparo à Pesquisa do Estado de Minas Gerais (FAPEMIG), by project APQ-00770-22, partially supported this study, and the Coordenação de Aperfeiçoamento de Pessoal de Nível Superior (CAPES) from Brazil for the doctorate scholarship. The Conselho Nacional de Desenvolvimento Científico e Tecnológico (CNPq) partially supported this study (project 406042/2022-5). The Núcleo Multiusuário from UFV – campus Florestal for atomic absorption analyses. The Centro de Microscopia daUFMG for the SEM/EDS images. The Laboratório multiusuários de Difração de raios-X from UFV – campus Rio Paranaíba for the XRD analyses.

Notes and references

1 F. Peterson and D. Wasley, *Phosphorus: Sources, Forms, Impact on Water Quality-A General Overview*, 2007.
2 J. Shen, L. Yuan, J. Zhang, H. Li, Z. Bai, X. Chen, W. Zhang and F. Zhang, Phosphorus dynamics: From soil to plant, *Plant Physiol.*, 2011, **156**, 997–1005.
3 V. J. G. Emídio, *A problemática do fósforo nas águas para consumo humano e águas residuais e soluções para o seu tratamento*, Universidade do Algarve, 2012, pp. 1–118.
4 H. Bacelo, A. M. A. Pintor, S. C. R. Santos, R. A. R. Boaventura and C. M. S. Botelho, Performance and prospects of different adsorbents for phosphorus uptake and recovery from water, *Chem. Eng. J.*, 2020, **381**, 122566.

5 P. Loganathan, S. Vigneswaran, J. Kandasamy and N. S. Bolan, *Crit. Rev. Environ. Sci. Technol.*, 2014, **44**, 847–907.
6 Y. Li, J. Shang, C. Zhang, W. Zhang, L. Niu, L. Wang and H. Zhang, The role of freshwater eutrophication in greenhouse gas emissions: A review, *Elsevier B.V.*, 2021, DOI: 10.1016/j.scitotenv.2020.144582.
7 O. Ruzhitskaya and E. Gogina, Methods for Removing of Phosphates from Wastewater 2 Sources of Phosphates Entering Water Reservoirs, *MATEC Web of Conferences*, 2017, pp. 1–7.
8 W. Gu, Q. Xie, C. Qi, L. Zhao and D. Wu, Phosphate removal using zinc ferrite synthesized through a facile solvothermal technique, *Powder Technol.*, 2016, **301**, 723–729.
9 D. Cordell, J. O. Drangert and S. White, *Glob. Environ. Change*, 2009, **19**, 292–305.
10 C. Klein and S. A. A. Agne, Fósforo: de nutriente à poluente!, *Elec. J. Manag. Educ. Environ. Technol.*, 2012, **8**, 1713–1721, DOI: 10.5902/223611706430.
11 S. Ahmed, M. N. Ashiq, D. Li, P. Tang, F. Leroux and Y. Feng, Recent Progress on Adsorption Materials for Phosphate Removal, *Recent Pat. Nanotechnol.*, 2019, **13**, 3–16.
12 Z. Ajmal, A. Muhmood, M. Usman, S. Kizito, J. Lu, R. Dong and S. Wu, Phosphate removal from aqueous solution using iron oxides: Adsorption, desorption and regeneration characteristics, *J. Colloid Interface Sci.*, 2018, **528**, 145–155.
13 Ü. Özgür, Y. Alivov and H. Morkoç, Microwave ferrites, part 1: fundamental properties, *J. Mater. Sci.:Mater. Electron.*, 2009, **20**, 789–834.
14 N. Kumari, R. Jasrotia, S. Kour, Neha, Y. Singh and R. Kumar, in *AIP Conference Proceedings*, American Institute of Physics Inc., 2022, vol. 2357.
15 R. C. Pullar, Hexagonal ferrites: A review of the synthesis, properties and applications of hexaferrite ceramics, *Prog. Mater. Sci.*, 2012, **57**, 1191–1334.
16 A. Vedrtnam, K. Kalauni, S. Dubey and A. Kumar, A comprehensive study on structure, properties, synthesis and characterization of ferrites, *AIMS Mater. Sci.*, 2020, **7**, 800–835.
17 A. Kalendová and D. Veselý, Needle-shaped anticorrosion pigments based on the ferrites of zinc, calcium and magnesium, *Anti-Corros. Methods Mater.*, 2007, **54**, 3–15.
18 D. H. K. Reddy and Y. S. Yun, Spinel ferrite magnetic adsorbents: Alternative future materials for water purification?, *Coord. Chem. Rev.*, 2016, **315**, 90–111.
19 R. A. Jasso-Terán, D. A. Cortés-Hernández, H. J. Sánchez-Fuentes, P. Y. Reyes-Rodríguez and L. E. León-Prado, Nanopartículas magnéticas de zinc y calcio para aplicaciones en hipertermia magnética, *Rev. Fac. Ing.*, 2016, **25**, 89–98.
20 W. Tang, Y. Su, Q. Li, S. Gao and J. K. Shang, Superparamagnetic magnesium ferrite nanoadsorbent for effective arsenic (III, V) removal and easy magnetic separation, *Water Res.*, 2013, **47**, 3624–3634.
21 M. Kaur, N. Kaur, K. Jeet and P. Kaur, MgFe2O4 nanoparticles loaded on activated charcoal for effective removal of Cr (VI) – A novel approach, *Ceram. Int.*, 2015, **41**, 13739–13750.
22 S. M. Ashekuzzaman and J. Q. Jiang, Study on the sorption-desorption-regeneration performance of Ca-, Mg- and CaMg-based layered double hydroxides for removing phosphate from water, *Chem. Eng. J.*, 2014, **246**, 97–105.
23 Y. Yang, Z. Cao, Y. Jiang, L. Liu and Y. Sun, Photoinduced structural transformation of SrFeO3 and Ca2Fe2O5 during photodegradation of methyl orange, *Mater. Sci. Eng., B*, 2006, **132**, 311–314.
24 P. Cheng, D. Chen, H. Liu, X. Zou, Z. Wu, J. Xie, C. Qing, D. Kong and T. Chen, Synergetic effects of anhydrite and brucite-periclase materials on phosphate removal from aqueous solution, *J. Mol. Liq.*, 2018, **254**, 145–153.
25 M. Silva and J. Baltrusaitis, A review of phosphate adsorption on Mg-containing materials: Kinetics, equilibrium, and mechanistic insights, *Environ. Sci.*, 2020, **6**, 3178–3194.
26 X. Liu, F. Shen and X. Qi, Adsorption recovery of phosphate from aqueous solution by CaO-biochar composites prepared from eggshell and rice straw, *Sci. Total Environ.*, 2019, **666**, 694–702.
27 M. H. P. Araújo, J. D. Ardisson, A. C. Krohling, R. M. Lago, W. Guimarães Júnior and J. C. Tristão, Calcium ferrites for phosphate adsorption and recovery from wastewater, *RSC Adv.*, 2024, **14**, 1612–1624.
28 R. Bhaumik, N. K. Mondal, B. Das, P. Roy, K. C. Pal, C. Das, A. Banerjee and J. K. Datta, Eggshell powder as an adsorbent for removal of fluoride from aqueous solution: equilibrium, kinetic and thermodynamic studies, *E-J. Chem.*, 2012, **9**, 1457–1480.
29 C. Han, J. Lalley, N. Iyanna and M. N. Nadagouda, Removal of phosphate using calcium and magnesium-modified iron-based adsorbents, *Mater. Chem. Phys.*, 2017, **198**, 115–124.
30 K. W. Jung, S. Lee and Y. J. Lee, Synthesis of novel magnesium ferrite ($MgFe_2O_4$)/biochar magnetic composites and its adsorption behavior for phosphate in aqueous solutions, *Bioresour. Technol.*, 2017, **245**, 751–759.
31 D. Mehta, S. Mazumdar and S. K. Singh, Magnetic adsorbents for the treatment of water/wastewater-A review, *Journal of Water Process Engineering*, 2015, **7**, 244–265.
32 T. Castelo-Grande, P. A. Augusto, J. Rico, J. Marcos, R. Iglesias, L. Hernández and D. Barbosa, Magnetic water treatment in a wastewater treatment plant: part I - sorption and magnetic particles, *J. Environ. Manage.*, 2020, **281**, 111872.
33 A. Eskandarpour, K. Sassa, Y. Bando, M. Okido and S. Asai, Magnetic removal of phosphate from wastewater using schwertmannite, *Mater. Trans.*, 2006, **47**, 1832–1837.
34 P. S. Kumar, L. Korving, M. C. M. van Loosdrecht and G. J. Witkamp, Adsorption as a technology to achieve ultra-low concentrations of phosphate: Research gaps and economic analysis, *Water Res.: X*, 2019, **4**, 100029.
35 Y. Wei, K. Guo, H. Wu, P. Yuan, D. Liu, P. Du, P. Chen, L. Wei and W. Chen, Highly regenerative and efficient adsorption of phosphate by restructuring natural palygorskite clayviaalkaline activation and co-calcination, *Chem. Commun.*, 2021, **57**, 1639–1642.

36 K. A. Tee, S. Ahmed, M. A. H. Badsha, K. C. J. Wong and I. M. C. Lo, Comprehensive review and future research directions on using various lanthanum-based adsorbents for selective phosphate removal, *Clean Technol. Environ. Policy*, 2023, **25**, 1–23.
37 A. Nuryadin and T. Imai, in *IOP Conference Series: Earth and Environmental Science*, IOP Publishing Ltd, 2021, vol. 926.
38 A. Ivanets, V. Prozorovich, M. Roshchina, T. Kouznetsova, N. Budeiko, L. Kulbitskaya, A. Hosseini-Bandegharaei, V. Masindi and V. Pankov, A comparative study on the synthesis of magnesium ferrite for the adsorption of metal ions: Insights into the essential role of crystallite size and surface hydroxyl groups, *Chem. Eng. J.*, 2021, **411**, 1–7.
39 M. J. Uddin and Y. K. Jeong, Adsorptive removal of pollutants from water using magnesium ferrite nanoadsorbent: a promising future material for water purification, *Environ. Sci. Pollut. Res.*, 2022, **29**, 9422–9447.
40 N. Doebelin and R. Kleeberg, Profex: A graphical user interface for the Rietveld refinement program BGMN, *J. Appl. Crystallogr.*, 2015, **48**, 1573–1580.
41 F. B. A. de Freitas, M. Y. d. F. Câmara and D. F. M. Freitas, Determinação do PCZ de adsorventes naturais utilizados na remoção de contaminantes em soluções aquosas, *Blucher Chemistry Proceedings 5o Encontro Regional de Química & 4o Encontro Nacional de Química*, 2015, vol. 3.
42 APHA, *Standard Methods for the Examination of Water and Waste Water*, American Public Health Association, Washington, DC, 22nd edn, 2012.
43 K. Deshpande, A. Mukasyan and A. Varma, Direct synthesis of iron oxide nanopowders by the combustion approach: Reaction mechanism and properties, *Chem. Mater.*, 2004, **16**, 4896–4904.
44 T. Pradita, S. J. Shih, B. B. Aji and Sudibyo, in *AIP Conference Proceedings*, American Institute of Physics Inc., 2017, vol. 1823.
45 J. Zhang, J. Uknalis, L. Chen, R. A. Moreau and H. Ngo, Development of magnesium oxide–zeolite catalysts for isomerization of fatty acids, *Catal. Lett.*, 2019, **149**, 303–312.
46 C. F. Holder and R. E. Schaak, Tutorial on powder x-ray diffraction for characterizing nanoscale materials, *ACS Nano*, 2019, **13**, 7359–7365.
47 S. I. Hussein, A. S. Elkady, M. M. Rashad, A. G. Mostafa and R. M. Megahid, Structural and magnetic properties of magnesium ferrite nanoparticles prepared via EDTA-based sol–gel reaction, *J. Magn. Magn. Mater.*, 2015, **379**, 9–15.
48 A. Pradeep, P. Priyadharsini and G. Chandrasekaran, Sol–gel route of synthesis of nanoparticles of $MgFe_2O_4$ and XRD, FTIR and VSM study, *J. Magn. Magn. Mater.*, 2008, **320**, 2774–2779.
49 R. Sagayaraj, A review on structural and magnetic properties of magnesium ferrite nanoparticles, *Int. Nano Lett.*, 2022, **12**, 345–350.
50 L. Mei, A. Iizuka and E. Shibata, Recent progress on utilization of metal-rich wastes in ferrite processing: a review, *Waste Biomass Valorization*, 2018, **9**, 1669–1679.
51 L. Wang, C. V. Putnis, J. Hövelmann and A. Putnis, Interfacial precipitation of phosphate on hematite and goethite, *Minerals*, 2018, 207.
52 J. Liu, R. Zhu, L. Ma, H. Fu, X. Lin, S. C. Parker and M. Molinari, Adsorption of phosphate and cadmium on iron (oxyhydr)oxides: A comparative study on ferrihydrite, goethite, and hematite, *Geoderma*, 2021, 114799.
53 M. Thommes, K. Kaneko, A. V. Neimark, J. P. Olivier, F. Rodriguez-Reinoso, J. Rouquerol and K. S. W. Sing, Physisorption of gases, with special reference to the evaluation of surface area and pore size distribution (IUPAC Technical Report), *Pure Appl. Chem.*, 2015, **87**, 1051–1069.
54 B. P. Ladgaonkar, C. B. Kolekar and A. S. Vaingankar, Infrared absorption spectroscopic study of Nd 3+ substituted Zn-Mg ferrites, *Bull. Mater. Sci.*, 2002, **25**, 351–354.
55 W. H. Lee and J. O. Kim, Phosphate recovery from anaerobic digestion effluent using synthetic magnetite particles, *J. Environ. Chem. Eng.*, 2022, 107103, DOI: 10.1016/j.jece.2021.107103.
56 V. Russo, M. Trifuoggi, M. Di Serio and R. Tesser, Fluid-solid adsorption in batch and continuous processing: a review and insights into modeling, *Chem. Eng. Technol.*, 2017, **40**, 799–820.
57 J. Wang and X. Guo, Adsorption isotherm models: classification, physical meaning, application and solving method, *Chemosphere*, 2020, **258**, 127279.
58 J. S. Piccin, T. R. S. A. Cadaval, L. A. A. De Pinto and G. L. Dotto, in *Adsorption Processes for Water Treatment and Purification*, Springer International Publishing, 2017, pp. 19–51.
59 K. Y. Foo and B. H. Hameed, Insights into the modeling of adsorption isotherm systems, *Chem. Eng. J.*, 2010, **156**, 2–10.
60 D. L. Peterson and O. Redlich, A useful adsorption isotherm, *Ind. Eng. Chew&., Anal. Ed*, 1945, **63**, 787.
61 C. R. Girish, Various isotherm models for multicomponent adsorption: A review, *Int. J. Civ. Eng. Technol.*, 2017, **8**, 80–86.
62 R. Farouq and N. S. Yousef, Equilibrium and Kinetics Studies of adsorption of Copper (II) Ions on Natural Biosorbent, *Int. J. Chem. Eng. Appl.*, 2015, **6**, 319–324.
63 M. Musah, Y. Azeh, J. Mathew, M. Umar, Z. Abdulhamid and A. Muhammad, Adsorption Kinetics and Isotherm Models: A Review, *Caliphate J. Sci. Technol.*, 2022, **4**, 20–26.
64 S. H. Chien and W. R. Clayton, Application of Elovich Equation to the Kinetics of Phosphate Release and Sorption in Soils 1, *Soil Sci. Soc. Am. J.*, 1977, **44**, 265–268.
65 A. Pavlatou and N. A. Polyzopoulos, The role of diffusion in the kinetics of phosphate desorption: the relevance of the Elovich equation, *J. Soil Sci.*, 1988, **39**, 425–436.
66 L. Largitte and R. Pasquier, A review of the kinetics adsorption models and their application to the adsorption of lead by an activated carbon, *Chem. Eng. Res. Des.*, 2016, **109**, 495–504.
67 W. A. House, F. H. Denison and P. D. Armitage, Comparison of the uptake of inorganic phosphorus to a suspended and stream bed-sediment, *Water Res.*, 1995, **29**, 767–779.

68 J. Torrent, Rapid and slow phosphate sorption by mediterranean soils: effect of iron oxides 1, *Soil Sci. Soc. Am. J.*, 1987, **51**, 78–82.

69 D. A. Almasri, N. B. Saleh, M. A. Atieh, G. McKay and S. Ahzi, Adsorption of phosphate on iron oxide doped halloysite nanotubes, *Sci. Rep.*, 2016, **9**(3232), 1–13.

70 N. Kaur, M. Kaur and D. Singh, Fabrication of mesoporous nanocomposite of graphene oxide with magnesium ferrite for efficient sequestration of Ni (II) and Pb (II) ions: Adsorption, thermodynamic and kinetic studies, *Environ. Pollut.*, 2019, **253**, 111–119.

71 N. J. Barrow and T. C. Shaw, Effects of ionic strength and nature of the cation on desorption of phosphate from soil, *Eur. J. Soil Sci.*, 1979, **30**, 53–65.

72 I. W. Almanassra, G. Mckay, V. Kochkodan, M. Ali Atieh and T. Al-Ansari, A state of the art review on phosphate removal from water by biochars, *Chem. Eng. J.*, 2021, **409**, 128211.

73 Y. Kashtan, M. Nicholson, C. J. Finnegan, Z. Ouyang, A. Garg, E. D. Lebel, S. T. Rowland, D. R. Michanowicz, J. Herrera, K. C. Nadeau and R. B. Jackson, Nitrogen dioxide exposure, health outcomes, and associated demographic disparities due to gas and propane combustion by U.S. stoves, *Sci. Adv.*, 2024, **10**, 8680.

74 J. Lalley, C. Han, X. Li, D. D. Dionysiou and M. N. Nadagouda, Phosphate adsorption using modified iron oxide-based sorbents in lake water: kinetics, equilibrium, and column tests, *Chem. Eng. J.*, 2016, **284**, 1386–1396.

75 C. Zhang, Y. Li, F. Wang, Z. Yu, J. Wei, Z. Yang, C. Ma, Z. Li, Z. Y. Xu and G. Zeng, Performance of magnetic zirconium-iron oxide nanoparticle in the removal of phosphate from aqueous solution, *Appl. Surf. Sci.*, 2017, **396**, 1783–1792.

76 Y. J. Tu and C. F. You, Phosphorus adsorption onto green synthesized nano-bimetal ferrites: Equilibrium, kinetic and thermodynamic investigation, *Chem. Eng. J.*, 2014, **251**, 285–292.

77 Z. Jia, Q. Wang, J. Liu, L. Xu and R. Zhu, Effective removal of phosphate from aqueous solution using mesoporous rodlike $NiFe_2O_4$ as magnetically separable adsorbent, *Colloids Surf., A*, 2013, **436**, 495–503.